



UNIVERSITY OF LEEDS

This is a repository copy of *Time-periodic forcing of spatially localized structures*.

White Rose Research Online URL for this paper:

<http://eprints.whiterose.ac.uk/93695/>

Version: Accepted Version

Article:

Gandhi, P, Beaume, C and Knobloch, E (2016) Time-periodic forcing of spatially localized structures. Springer Proceedings in Physics, 173. pp. 303-316. ISSN 0930-8989

https://doi.org/10.1007/978-3-319-24871-4_23

© 2016, Springer International Publishing Switzerland. This is an author produced version of a paper published in Springer Proceedings in Physics. Uploaded in accordance with the publisher's self-archiving policy. The final publication is available at Springer via http://dx.doi.org/10.1007/978-3-319-24871-4_23

Reuse

Unless indicated otherwise, fulltext items are protected by copyright with all rights reserved. The copyright exception in section 29 of the Copyright, Designs and Patents Act 1988 allows the making of a single copy solely for the purpose of non-commercial research or private study within the limits of fair dealing. The publisher or other rights-holder may allow further reproduction and re-use of this version - refer to the White Rose Research Online record for this item. Where records identify the publisher as the copyright holder, users can verify any specific terms of use on the publisher's website.

Takedown

If you consider content in White Rose Research Online to be in breach of UK law, please notify us by emailing eprints@whiterose.ac.uk including the URL of the record and the reason for the withdrawal request.



eprints@whiterose.ac.uk
<https://eprints.whiterose.ac.uk/>

Time-periodic forcing of spatially localized structures

Punit Gandhi, Cédric Beaume, and Edgar Knobloch

Abstract We study localized states in the Swift–Hohenberg equation when time-periodic parametric forcing is introduced. The presence of a time-dependent forcing introduces a new characteristic time which creates a series of resonances with the depinning time of the fronts bounding the localized pattern. The organization of these resonances in parameter space can be understood using appropriate asymptotics. A number of distinct canard trajectories involved in the observed transitions are constructed.

1 Introduction

Fourth order reversible systems capture the behavior of a host of systems in physics, chemistry, and biology [9, 21] that exhibit localized structures in the form of a time-independent patch of pattern embedded in a homogenous background. Examples of systems that support localized structures of this type include buckling of slender structures [18, 19], ferrofluids [30], shear flows [32], convection [26, 2, 3, 4, 5, 20], nonlinear optical media [12], urban criminal behavior [34, 24] and desert vegetation [33, 36]. We consider the following Swift–Hohenberg equation (SHE):

$$u_t = ru - (1 + \partial_x^2)^2 u + bu^2 - u^3, \quad (1)$$

Punit Gandhi
Department of Physics, University of California, Berkeley CA 94720, USA, e-mail: punit_gandhi@berkeley.edu

Cédric Beaume
Department of Aeronautics, Imperial College London, London SW7 2AZ, UK e-mail: ced.beaume@gmail.com

Edgar Knobloch
Department of Physics, University of California, Berkeley CA 94720, USA, e-mail: knobloch@berkeley.edu

where $u(x, t)$ is a real scalar field, r is a forcing parameter, and $b > 0$ is a constant. The Swift–Hohenberg equation provides an excellent qualitative description of spatially localized structures in the systems mentioned above. These solutions live on a pair of branches that *snake* within a snaking or pinning parameter interval. Analysis reveals that within this interval a large number of such states can be simultaneously stable [8, 22].

We consider the SHE (1) on a sufficiently long spatially periodic domain, and set $b = 1.8$ so that, for constant forcing, there exists an interval $r_{sn} \leq r \leq 0$ of bistability between the trivial $u \equiv 0$ state and a spatially periodic state $u = u_P(x)$ with $r_{sn} \approx -0.3744$. We characterize localized states comprised of a patch of u_P embedded in a $u = 0$ background through the location $x = f$ of the front that defines their right edge relative to their center $x = 0$:

$$f = 2 \frac{\int_0^{\Gamma/2} x u^2 dx}{\int_0^{\Gamma/2} u^2 dx}. \quad (2)$$

For forcing between $r_- \approx -0.3390$ and $r_+ \approx -0.2593$, the dynamics is organized around a series of stable localized solutions in which the fronts remain pinned at locations an integer number of wavelengths of u_P apart. The fronts of a localized initial condition within the pinning interval will move either inward or outward until f reaches a value corresponding to a stable state. Outside the pinning interval but inside the bistability interval, the fronts are no longer pinned and the localized patterns either steadily expand ($r_+ < r < 0$) or shrink ($r_{sn} < r < r_-$) via repeated wavelength nucleation or annihilation. In both cases, the average speed of the front increases monotonically with the distance to the pinning interval.

Near the edge of the pinning interval, leading order asymptotic theory [8] predicts that the time to nucleate or annihilate a wavelength of the pattern on either side is given by $(T_{\pm}^{\text{dnp}})^{-1} \approx \Omega_{\pm} \sqrt{|r - r_{\pm}|} / \pi$ when $0 < \pm(r - r_{\pm}) \ll 1$. We have used the subscript $+$ (resp. $-$) for nucleation (resp. annihilation) events on the right (resp. left) of the pinning interval. For quantitatively accurate predictions of the depinning time outside of this limit, we employ the following numerical fit [13]:

$$\left(T_{\pm}^{\text{dnp}}\right)^{-1} = \sum_{j=1}^5 \sigma_j^{\pm} |r_0 - r_{\pm}|^{\frac{j}{2}}. \quad (3)$$

where the coefficients σ_j^{\pm} are obtained from simulations of SHE with constant forcing (Table 1).

To the left of the bistability interval (i.e., for $r < r_{sn}$), the dynamics of localized states is better described by overall amplitude decay, and we use a numerical fit of the form (3) to quantify the amplitude collapse time T_{sn}^{col} of a periodic solution below r_{sn} in terms of $|r - r_{sn}|$.

In practice, the forcing can fluctuate in time and induce the creation of new states [38, 25, 6]. Systems can be noisy [31, 29, 1] leading to front propagation [10] or temporally periodic [37, 23, 7] providing control opportunities [35]. We focus here on the dynamics of pre-existing localized structures under the influence of time-

	Ω	σ_1	σ_2	σ_3	σ_4	σ_5
T_+^{dnpn}	0.5285	0.1687	0.1141	0.7709	-0.4000	0.0803
T_-^{dnpn}	0.7519	0.2381	-0.8445	33.37	-306.4	1067
T_{sn}^{col}	0.7705	0.2081	0.4431	2.962	-34.15	79.52

Table 1 Values of the coefficients σ_j determined from a least squares fit of the depinning/collapse time to simulations of spatially localized initial conditions with constant forcing. The frequency Ω is calculated from leading order asymptotic theory [8] for perturbations of localized states that are marginally stable at r_{\pm} and periodic states that are marginally stable at r_{sn} .

periodic forcing. The effect of such oscillations on the growth of vegetation patches near the transition to desertification is of particular interest: over the course of a year, seasonal variations may place the system alternately within conditions where only the bare soil state is stable and within conditions where bistability between bare soil and vegetation patterns is observed. Steady models of this process predict the presence of patchy patterns [28] and only limited results are available on their reaction to time-dependence in external conditions [39, 14].

We introduce the time-periodic forcing in the simplest way:

$$r(t) = r_0 + \rho \sin(2\pi t/T), \quad (4)$$

where $r(t)$ is hereafter referred to as the forcing parameter and restrict attention to localized structures satisfying reflection symmetry: $u(x) \rightarrow u(-x)$. The oscillation amplitude ρ is chosen to straddle the snaking interval $r_- \leq r_0 \leq r_+$ with $\rho > (r_+ - r_-)/2$ and $T > 0$. The time-dependent forcing may cause the localized patterns to breathe, or grow for part of the cycle via nucleation of new wavelengths of the pattern followed by wavelength annihilation during the remainder of the cycle as we shall see. The period of the forcing, T , introduces a new characteristic time in the system that interacts with the depinning time to create resonances. The origin of these resonances as well as their impact on the way parameter space is structured is described in the next section. Section 4 discusses a class of peculiar periodic orbits called canard orbits that are involved in the observed transitions. The paper concludes in section 5.

2 Temporal resonances

To understand the series of resonances underpinning the partitioning of the parameter space described below, we begin by considering the effects of an asymptotically small forcing amplitudes $\rho \ll 1$ when r_0 is located near one of the edges of the pinning interval ($|r_0 - r_{\pm}| \ll 1$). When $(r_0 - r_{\pm})/\rho$ is finite the depinning time scales like $\sim |r_0 - r_{\pm}|^{-1/2}$ and we therefore choose a forcing period such that $\sqrt{\rho}T \sim \mathcal{O}(1)$ in order to allow enough time for depinning to occur while the system is outside of the constant r pinning interval. It turns out that this limit is described, after appropriate transformation, by the Mathieu equation [13] which captures precisely the

periodicity of the nucleation process in the frame of the front. This equation predicts a set of resonance bands within an $\mathcal{O}(\rho)$ vicinity of either edge of the pinning interval. The resonances occur when the system spends an integer number of nucleation times outside of the constant r pinning interval. The r -dependence of the depinning time (3) allows the resonance bands to persist even when the system remains outside the constant r pinning interval throughout the entire forcing cycle.

Fig. 1 Resonance bands (white) in the (r_0, T) plane obtained from the Mathieu description [13]. Localized states that are marginally stable at $r = r_{\pm}$ undergo a fixed number of depinning events per forcing cycle within each resonance band. This number is indicated in the most prominent bands. The transition zones (gray) indicate parameter values where the average number of depinning events per forcing cycle is non-integer.

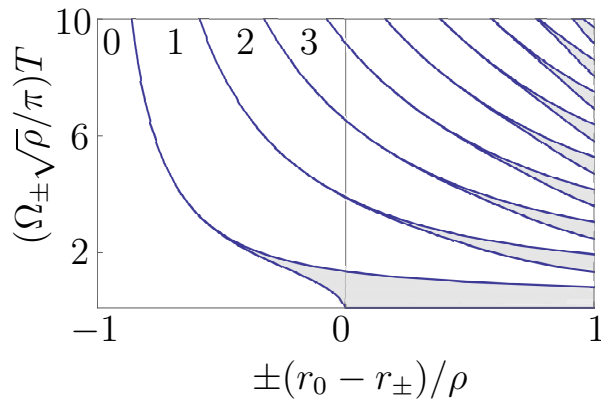


Figure 1 shows the predicted dynamics of a localized state that is marginally stable at $r = r_{\pm}$ with periodic forcing (4) in terms of $\sqrt{\rho}T$ (in units of π/Ω_{\pm}) and $\pm(r_0 - r_{\pm})/\rho$. A series of resonance bands (shown in white) separated by transition zones (shown in gray) is observed. In each of these bands, the number of depinning events per forcing cycle is locked to an integer number, starting with 0 for the left-most band, and increasing by 1 for each successive band. The transition zones indicate parameters with a non-integer average number of depinning events per forcing cycle, resulting either in periodic motion with period greater than T or nonperiodic motion [13].

2.1 Creation of sweet spots and pinched zones

We can analyze the interaction between the resonance bands occurring at either edge of the pinning interval in the following asymptotic limit. We tune the amplitude and average value of the forcing such that the extrema of the forcing remain within an asymptotically small vicinity of the edges of the pinning interval: $|\rho - p| \ll 1$, where $p = (r_+ + r_-)/2$, and assume $|r_0 - r_c| \ll 1$, where $r_c = (r_+ + r_-)/2$ is the center of the pinning interval, so that $|\rho - p|/|r_0 - r_c| \sim \mathcal{O}(1)$. Additionally, we choose the period of the forcing cycle such that $|\rho - p|T \sim \mathcal{O}(1)$ in order to obtain slow-fast dynamics involving slow drifts along the constant forcing localized state branch separated by fast depinning events.

This limit predicts the number of nucleation events n_+ and annihilation events $-n_-$ during one forcing period [13]:

$$n_{\pm} = \begin{cases} \left[\frac{\Omega_{\pm} T}{2\pi\sqrt{2p}} (r_0 \pm \rho - r_{\pm}) \right] & \text{if } \pm (r_0 \pm \rho - r_{\pm}) > 0 \\ 0 & \text{if } \pm (r_0 \pm \rho - r_{\pm}) \leq 0 \end{cases}, \quad (5)$$

where the brackets indicate rounding to the nearest integer and come from the settling of the state to a stable localized solution upon re-entry into the pinning interval.

For $\rho - p < 0$, the resonance bands associated with the left and right edges of the pinning interval are disjoint but asymptotically approach $r_0 = r_c$ as $T \rightarrow \infty$ for $\rho = p$. For $\rho - p > 0$, an asymptotically small sweet spot and pinching structure begins to form as a result of successive crossing between the resonance bands, as shown in Figure 2.

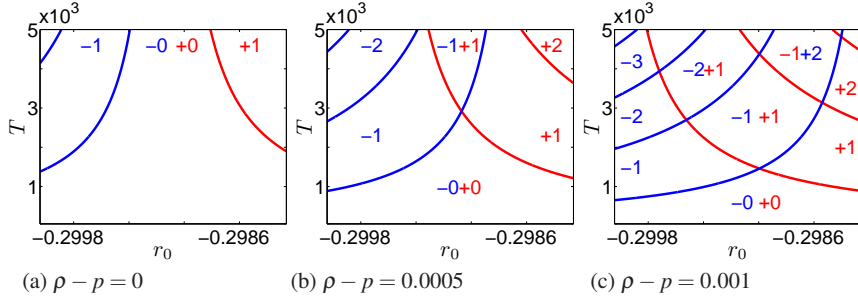


Fig. 2 Predictions from the asymptotic theory, Eq. (5). The blue (resp. red) lines correspond to parameter values where n_- (resp. n_+) changes.

2.2 Phase space partitioning

We ran simulations for $\rho = 0.1$ and $10 \leq T \leq 400$, initialized with a stable steady-state localized solution at $r(t=0)$. The simulations revealed four different behaviors that we exemplify in Figure 3. The localized structure expands (f increases) by the nucleation of new wavelengths on either side of the pattern when $r > r_+$ while it contracts (f decreases) by the decay of side wavelengths when $r < r_-$. In the case $r < r_{sn}$, an overall amplitude decay mode kicks in that can destroy the localized state within a single forcing period. We can therefore observe growing (figure 3(a)), decaying solutions (figure 3(c)) or collapse to the trivial state (figure 3(d)). When not enough time is spent below r_{sn} , the dynamics can be balanced by suitably choosing the parameter values and spatially localized periodic orbits can be obtained (figure 3(b)).

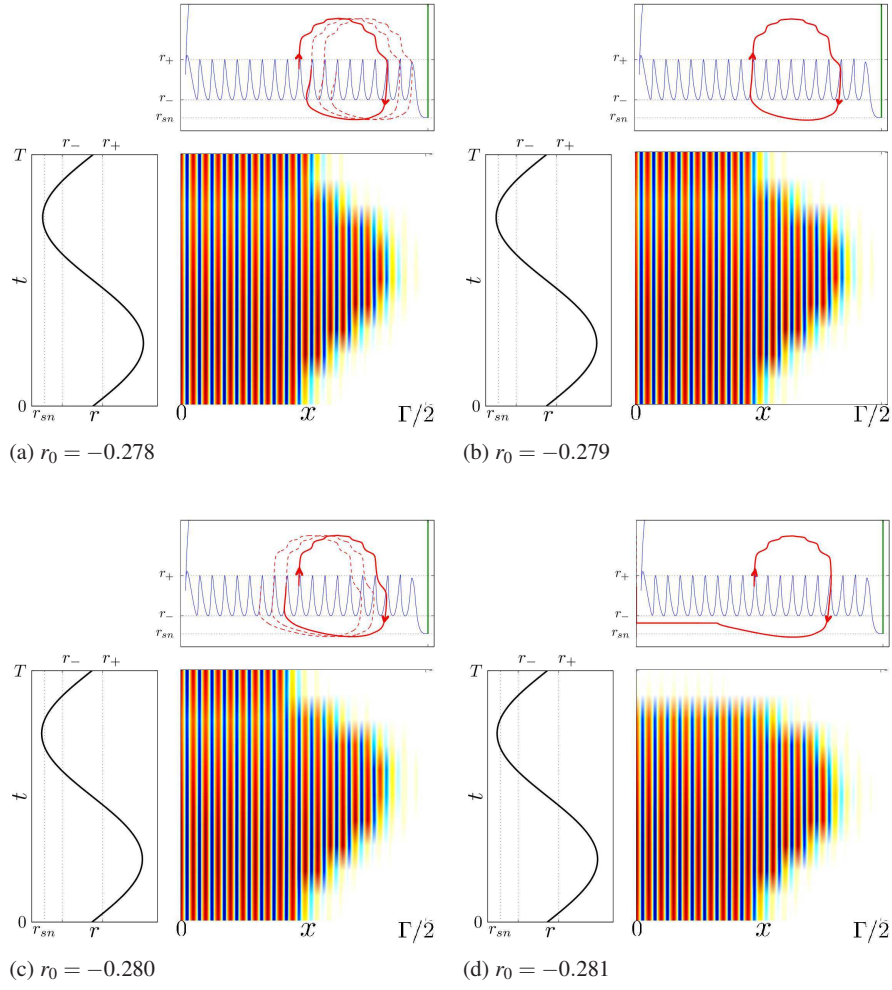


Fig. 3 Breathing localized structures observed in a periodic domain of size $\Gamma = 80\pi$ in the SHE (1) with the forcing (4) for $\rho = 0.1$, $T = 300$, $b = 1.8$ and different values of r_0 . Left panels: the forcing r represented as a function of time with thin dashed lines indicating the boundaries of the pinning and bistability regions. Right panels: space-time diagrams over one forcing cycle for the right half of each state with positive (negative) values of the field u shown in red (blue). Top panels: trajectories of the position $x = f$ of the right front of the localized state in (f, r) space superposed on the constant forcing snaking diagram.

We characterize the results in a (r_0, T) diagram through the average motion of the fronts per forcing cycle:

$$\langle \Delta f \rangle = \frac{f(t = t_0 + N_t T) - f(t = t_0)}{N_t}, \quad (6)$$

where t_0 is large enough to bypass initial transients and N_t is a large number of forcing cycles over which the dynamics is averaged. The numerical results are reported in figure 4(a). Periodic orbits exist in the region PO that displays a series of contrac-

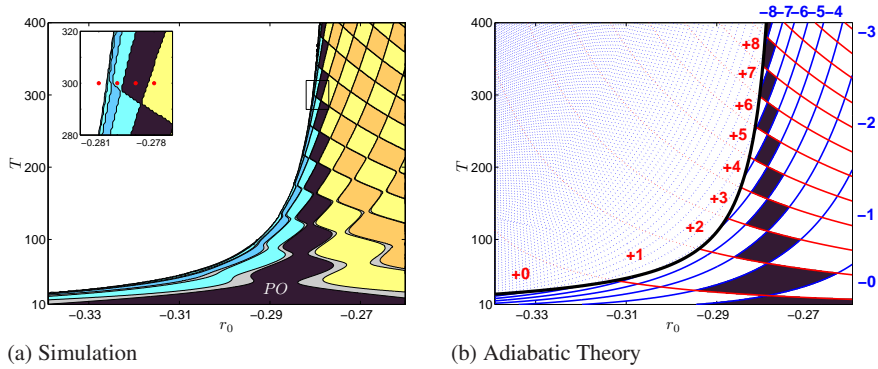


Fig. 4 (a) Color map of the different behaviors observed from simulations in the (r_0, T) plane for $\rho = 0.1$ and $b = 1.8$ [13]. Periodic orbits exist within region PO . The yellow/orange (light blue/blue) regions to the right (left) of PO correspond growing (decaying) solutions where the pattern experiences net growth (decay) by $1, 2, \dots$ wavelengths on either side per cycle. All regions are defined by $-0.25 + N < \langle \Delta f \rangle / 2\pi < 0.25 + N$ with $\pm N \in \mathbb{N}$. We note that a more stringent definition would produce slightly narrower regions, particularly for shorter periods, but qualitatively similar. Transition zones are shown in gray. The white region indicates parameter values at which the amplitude of the localized pattern decays within one cycle independently of its original length. The inset shows the location of the simulations shown in Fig. 3. (b) The red (blue) lines show predictions from Eq. (7). The bands are labeled with red (blue) signed integers, and the thick black line marks the prediction of the cliff beyond which amplitude decay is expected. Both panels are plotted over the static pinning interval $r_- < r_0 < r_+$.

tions and expansions and progressively shrinks as T increases. Around this region, similarly shaped regions display states that expand or shrink over time. They are structured in a regular fashion: the region right next to PO displays states that grow or decay by one wavelength on each side of the pattern during each forcing cycle, and farther regions display successively faster growing or decaying states. The transition between each of these regions is not abrupt and occurs via transition zones (shown in gray in (a)) [13] that are beyond the scope of the present paper.

With constant forcing, one can approximate the signed number of depinning events that occur outside of the pinning interval by integrating the depinning rate over the time of interest:

$$n_{\pm} = \pm \int \frac{dt}{T_{\pm}^{\text{dpn}}(r)}. \quad (7)$$

In the limit $T \rightarrow \infty$, we can treat the parameter $r(t)$ quasi-statically and make use of Eq. (3) for T_{\pm}^{dpn} . We construct an adiabatic prediction by assuming the following series of events during each forcing cycle:

- $r > r_+$: the localized state begins to nucleate wavelengths of the pattern. We count the total number of depinning events using positive real numbers $n_+ > 0$ obtained from Eq. (7) using Eq. (3) and Table 1.
- $r_+ > r > r_-$: Upon entry into the pinning interval, the state converges to the closest stable localized solution, corresponding to rounding n_+ or n_- to the nearest integer $[n_+]$ or $[n_-]$.
- $r < r_-$: We count the number of wavelengths annihilated on either side using negative real numbers $n_- < 0$ also obtained from Eq. (7). If the time spent with $r < r_{sn}$ exceeds that required for $\int_{r < r_{sn}} (T^{\text{col}}(r(t)))^{-1} dt = 1/2$, then the state decays irrevocably.

Figure 4(b) shows that this prediction bears a striking resemblance to the numerical results in figure 4(a). In fact, most of the features obtained during simulations can be explained using the adiabatic theory even far away from the limit for which it is constructed [14, 13]. The series of contractions and expansions observed in the numerical simulation is therefore a trace of the sweet spot and pinching structure and come from the fact that any incomplete growth or decay of a wavelength is canceled or completed as the forcing parameter reenters the pinning interval.

3 Canard trajectories

We have, up to this point, described *stable* localized breathing states that we obtained by time-stepping a *stable* steady-state solution to Eq. (1) with constant forcing $r = r_0$. As the snaking structure indicates, each stable localized state is connected to the next one by a branch of unstable localized states. These unstable states also generate spatially localized periodic orbits under periodic forcing. These orbits are similar to those presented in the last section but instead of tracking the stable part of the snaking branches as the forcing is varied, they track the unstable part and are therefore unstable as well.

Near the transition between neighboring resonance bands in figure 2, one can find trajectories that follow a stable snaking branch during one traversal of the pinning interval and an unstable one during the return trip. A small change in parameter values can cause the trajectory to jump to one of the two nearby stable solution branches during its passage along the unstable branch before completing the journey across the pinning interval. During such a jump the fronts bounding the localized state will either move outward or inward depending on whether the stable state reached is longer or shorter than the unstable state. In the following we refer to

trajectories that drift along unstable states for part of the forcing cycle as *canard* trajectories [11].

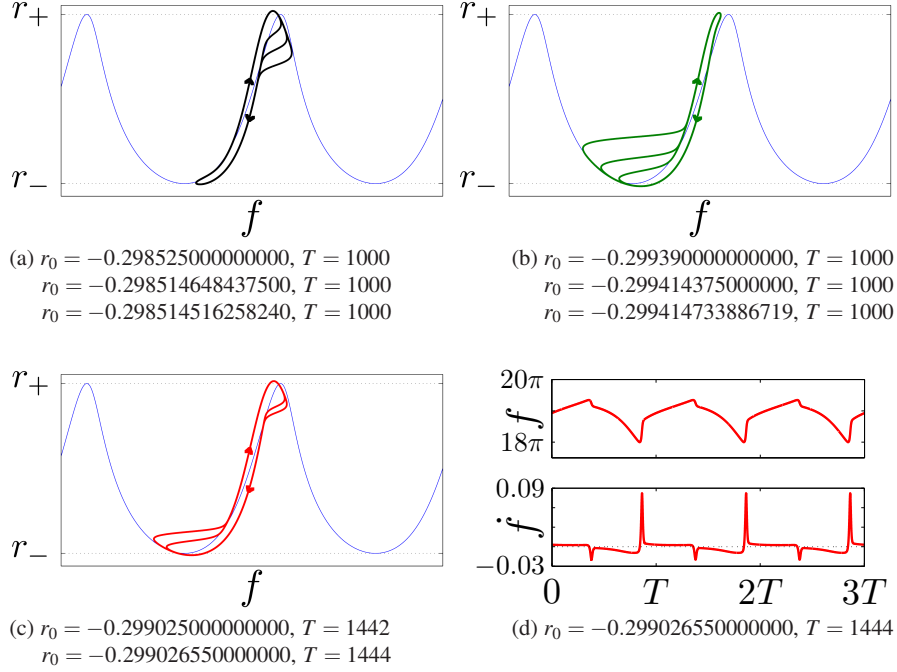
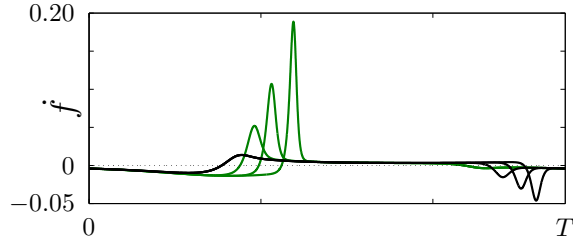


Fig. 5 (a) C_+ canards, (b) C_- canards and (c) C^\pm canards represented through the front location f versus the forcing strength $r(t)$ for $\rho - p = 0.001$ (Fig. 2(c)). The thin blue line represents the stable ($\partial_f r > 0$) and unstable ($\partial_f r < 0$) parts of the branch of localized solutions for constant forcing ($\rho = 0$). In each case the parameters are listed in order of increasing time spent on the unstable branch. (d) Three periods of a C^\pm canard from panel (c) shown using the front location $x = f$ and its speed \dot{f} as functions of time.

It is possible to control how far along the unstable solution branch the system reaches before jumping to a stable branch and thereby generate a family of canard trajectories. Figure 5 shows three families of periodic canard trajectories computed from Eq. (1) such that $\|u(t) - u(t+T)\|_{L^2} < 10^{-10}$ for some sufficiently large t . Solutions in the family of C^+ canards follow the unstable branch close to the saddle-node at $r = r_+$ but deviate before reaching the saddle-node at $r = r_-$ (panel (a)). Solutions of this type are found near the transition between one growth band and the next. The C_- canards shown in panel (b) follow the unstable branch close to the r_- saddle-node but do not reach the r_+ saddle-node; these are found near transitions between adjacent decay bands. Both sets of transitions are approximated by Eq. (5). In regions where both bands intersect, it is possible to obtain C^\pm canards (panel (c)) which temporarily follow two different unstable branches; the associated front location $x = f$ and its speed \dot{f} is represented in panels (d). When the trajectory is

drifting along the branch of steady states the fronts move slowly inward or outward; however, the jumps from the unstable state to the stable state manifest themselves in abrupt changes in the front location, or equivalently in dramatic peaks in the front speed \dot{f} . Figure 6 shows how a small change in r_0 (T remaining fixed) impacts the time evolution of canard trajectories. Decreasing r_0 delays the onset of the bursts and

Fig. 6 One period of the C_- (green) and C^+ (black) canards from Fig. 5(a) and Fig. 5(b) represented through the speed \dot{f} of the right front as a function of time. The larger amplitude peaks are associated with the larger canards in Fig. 5.



increases the front speed, a consequence of the fact that the trajectory now departs from an unstable state farther from the saddle-node and hence with a larger unstable eigenvalue. However, canards that manage to traverse almost the entire unstable part of the branch of steady states are expected to display once again slower dynamics.

The canards shown in figure 5 correspond to the simplest canard families, organized by a single stable portion of the branch of steady states with no depinning. However, a careful tuning of the parameters reveals the presence of canards displaying depinning. Figure 7 shows several examples of the corresponding trajectories.

The periodic orbits described by these canards are organized around *two* segments of stable steady states and the adjacent unstable steady states. The transitions between these segments are associated with the addition or loss of one wavelength on either side of the localized structure. A whole flock of canards can thus be obtained involving more and more segments of stable states and therefore displaying more depinning events per cycle.

In a similar fashion, we can obtain periodic orbits whose solution amplitude follows that of the lower branch spatially periodic state of the steady SHE. This gives rise to C_- canards characterized by a monotonic decrease in amplitude followed by a sudden jump to larger amplitude. Since the spatially periodic state u_p only displays one saddle-node no C^+ or C_-^+ canards can be obtained. These canard trajectories, represented in figure 8 (left panel), can be made to follow the unstable periodic state for a longer amount of time by choosing r_0 closer to the transition to amplitude collapse. Such trajectories spend more time in the depinning regime ($r < r_-$) as well as more time in the collapse regime ($r < r_{sn}$). As a result this regime is characterized by a competition between depinning and amplitude collapse as illustrated in figure 9 but the state ultimately always collapses as exemplified by the spiraling trajectory in figure 8 (right panel).

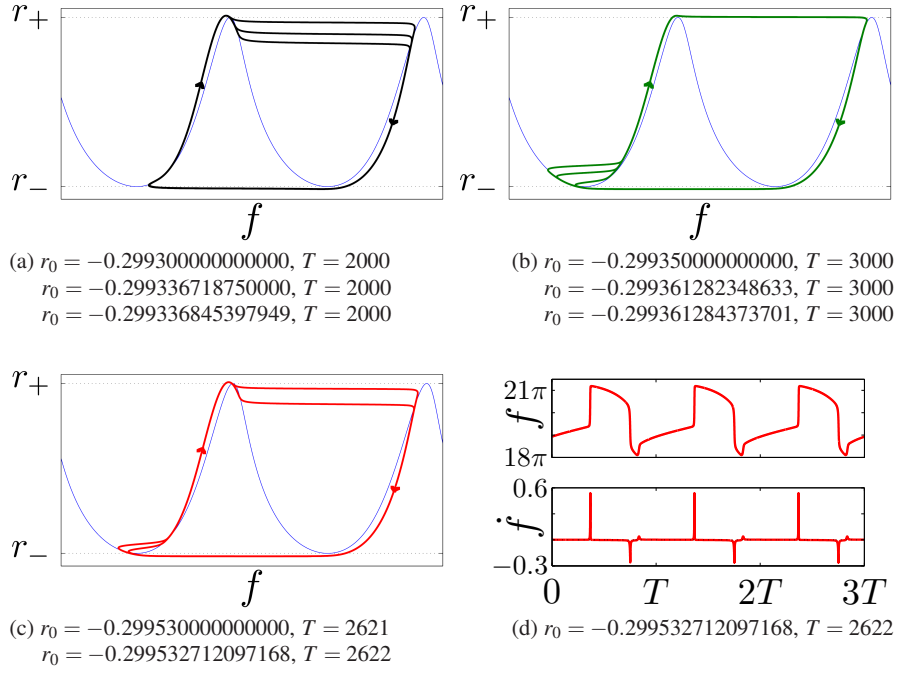


Fig. 7 “Larger” canards represented in the same fashion as in Fig. 5.

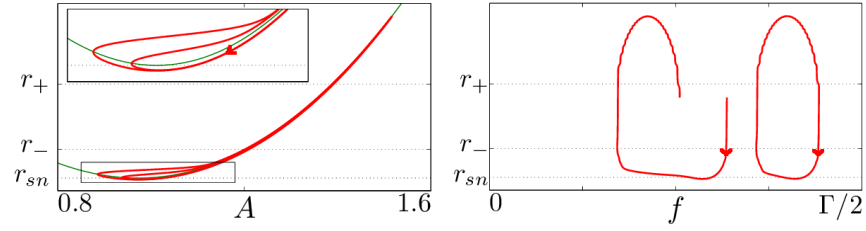


Fig. 8 Amplitude and front position of canard trajectories of spatially *localized* states that follow the unstable amplitude of the spatially *periodic* state u_p for some amount of time. Here $\rho = -0.1$, $r_0 = -0.276055$, -0.276220 , $T = 1100$, and $\Gamma = 640\pi$. The fold on the u_p branch is at $r_{sn} \approx -0.374370$.

4 Discussion

In this paper, we have used the SHE with a sinusoidal time-periodic forcing to describe how steady localized states are impacted by temporal variations in a parameter that temporarily take them outside their existence range. Numerical simulations complemented with asymptotic predictions were used to determine the location in parameter space of time-periodic spatially localized states and to reveal an unexpected sweet spot–pinching structure in the (r_0, T) plane for a fixed amplitude ρ of

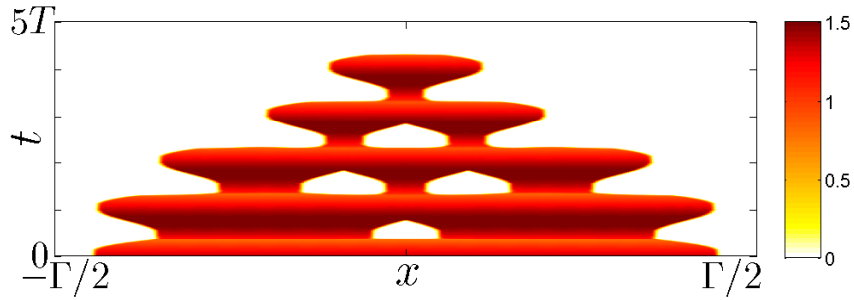


Fig. 9 Space-time plot of an amplitude canard trajectory similar to the shrinking canard seen in Fig. 8. Here, new fronts are generated in the interior in addition to the breathing dynamics on the edges. Parameters are $\rho = -0.1$, $r_0 = -0.276228387$, $T = 1100$, and $\Gamma = 640\pi$. Owing to the large extent of the domain, the pattern is not fully represented, only its local maxima are plotted against time.

the forcing. This structure is a consequence of a series of resonances between the forcing period and the nucleation time for new cells outside the pinning interval, and can be reproduced accurately using adiabatic theory as summarized in Eq. (7). Close to the resonance bands, a series of canard trajectories can be found. Two types of canards have been identified: phase canards, in which the spatial extent of the localized pattern changes abruptly as an additional wavelength is nucleated or annihilated on either side, and amplitude canards, in which the amplitude temporarily drops to the amplitude of the unstable lower branch of spatially periodic states before abruptly increasing to the amplitude of the stable upper states. Canards are normally considered to be a property of finite-dimensional systems, although there are indications that they should be observable in pattern-forming (i.e., spatially extended) systems and in particular in the Faraday system [16]. It is therefore of particular interest to present clear evidence for such orbits in a partial differential equation.

The Swift–Hohenberg equation provides a dependable framework for studies and control of the dynamics of spatially localized states as proved time and time again [17, 27]. For this reason the robustness of the resonance structure predicted by adiabatic theory for parameter values far from the adiabatic limit leads us to expect similar dynamics in related systems, and in particular in models of desert vegetation [39]. The reason for this expectation is that the phenomena described here are fundamentally low-dimensional. Indeed, a similar series of resonances is present in a simple ordinary differential equation, the periodically forced Adler equation, as described elsewhere [15].

Acknowledgment. This work was supported by the National Science Foundation under grant CMMI–1233692.

References

1. D. Barkley and L. S. Tuckerman. Computational study of turbulent laminar patterns in Couette flow. *Phys. Rev. Lett.*, 94:014502, 2005.
2. C. Beaume, A. Bergeon, H.-C. Kao, and E. Knobloch. Convectons in a rotating fluid layer. *J. Fluid Mech.*, 717:417–448, 2013.
3. C. Beaume, A. Bergeon, and E. Knobloch. Convectons and secondary snaking in three-dimensional natural doubly diffusive convection. *Phys. Fluids*, 25:024105, 2013.
4. C. Beaume, H.-C. Kao, E. Knobloch, and A. Bergeon. Localized rotating convection with no-slip boundary conditions. *Phys. Fluids*, 25:124105, 2013.
5. C. Beaume, E. Knobloch, and A. Bergeon. Nonsnaking doubly diffusive convectons and the twist instability. *Phys. Fluids*, 25:114102, 2013.
6. I. Belykh, V. Belykh, R. Jeter, and M. Hasler. Multistable randomly switching oscillators: The odds of meeting a ghost. *Euro. Phys. J. Special Topics*, 222:2497–2507, 2013.
7. P. Binder, D. Abraimov, A. V. Ustinov, S. Flach, and Y. Zolotaryuk. Observation of breathers in Josephson ladders. *Phys. Rev. Lett.*, 84:745–748, 2000.
8. J. Burke and E. Knobloch. Localized states in the generalized Swift-Hohenberg equation. *Phys. Rev. E*, 73:056211, 2006.
9. A. R. Champneys. Homoclinic orbits in reversible systems and their applications in mechanics, fluids and optics. *Physica D*, 112:158–186, 1998.
10. M. G. Clerc, C. Falcon, and E. Tirapegui. Additive noise induces front propagation. *Phys. Rev. Lett.*, 94:148302, 2005.
11. W. Eckhaus. Relaxation oscillations, including a standard chase on French ducks. In *Asymptotic Analysis II*, volume 985 of *Lecture Notes in Mathematics*, pages 449–494. Springer, New York, 1983.
12. W. J. Firth, L. Columbo, and A. J. Scroggie. Proposed resolution of theory-experiment discrepancy in homoclinic snaking. *Phys. Rev. Lett.*, 99:104503, 2007.
13. P. Gandhi, C. Beaume, and E. Knobloch. A new resonance mechanism in the Swift-Hohenberg equation with time-periodic forcing. *SIAM J. Appl. Dyn. Sys.*, 14:860–892, 2015.
14. P. Gandhi, E. Knobloch, and C. Beaume. Localized states in periodically forced systems. *Phys. Rev. Lett.*, 114:034102, 2015.
15. P. Gandhi, E. Knobloch, and C. Beaume. Phase-locking in modulated systems. *Phys. Rev. E*, page to appear, 2015.
16. M. Higuera, E. Knobloch, and J. M. Vega. Dynamics of nearly inviscid Faraday waves in almost circular containers. *Physica D*, 201:83–120, 2005.
17. S. M. Houghton and E. Knobloch. Swift-Hohenberg equation with broken cubic-quintic nonlinearity. *Phys. Rev. E*, 84:016204, 2011.
18. G. W. Hunt, H. M. Bolt, and J. M. T. Thompson. Structural localization phenomena and the dynamical phase-space analogy. *Proc. R. Soc. London A*, 425:245–267, 1989.
19. G. W. Hunt, M. A. Peletier, A. R. Champneys, P. D. Woods, M. A. Wadee, C. J. Budd, and G. J. Lord. Cellular buckling in long structures. *Nonlinear Dynamics*, 21:3–29, 2000.
20. D. Lo Jacono, A. Bergeon, and E. Knobloch. Three-dimensional binary fluid convection in a porous medium. *J. Fluid Mech.*, 730:R2, 2013.
21. E. Knobloch. Spatially localized structures in dissipative systems: open problems. *Nonlinearity*, 21:T45–T60, 2008.
22. E. Knobloch. Spatial localization in dissipative systems. *Annu. Rev. Condens. Matter Phys.*, 6:325–59, 2015.
23. O. Lioubashevski, Y. Hamiel, A. Agnon, Z. Reches, and J. Fineberg. Oscillons and propagating solitary waves in a vertically vibrated colloidal suspension. *Phys. Rev. Lett.*, 83:3190–3193, 1999.
24. D. J. B. Lloyd and H. O’Farrell. On localised hotspots of an urban crime model. *Physica D*, 253:23–39, 2013.
25. B. Marts, A. Hagberg, E. Meron, and A. L. Lin. Resonant and nonresonant patterns in forced oscillators. *Chaos*, 16:037113, 2006.

26. I. Mercader, O. Batiste, A. Alonso, and E. Knobloch. Convectons, anticonvectons and multi-convectons in binary fluid convection. *J. Fluid Mech.*, 667:586–606, 2011.
27. I. Mercader, O. Batiste, A. Alonso, and E. Knobloch. Travelling convectons in binary fluid convection. *J. Fluid Mech.*, 772:240–266, 2013.
28. E. Meron. Pattern-formation approach to modelling spatially extended ecosystems. *Ecol. Model.*, 234:70–82, 2012.
29. A. Prigent, G. Grégoire, H. Chaté, O. Dauchot, and W. van Saarloos. Large-scale finite-wavelength modulation within turbulent shear flows. *Phys. Rev. Lett.*, 89:014501, 2002.
30. R. Richter and I. V. Barashenkov. Two-dimensional solitons on the surface of magnetic fluids. *Phys. Rev. Lett.*, 94:184503, 2005.
31. B. Schäpers, M. Feldmann, T. Ackemann, and W. Lange. Interaction of localized structures in an optical pattern-forming system. *Phys. Rev. Lett.*, 85:748–751, 2000.
32. T. M. Schneider, J. Gibson, and J. Burke. Snakes and ladders: localized solutions of plane Couette flow. *Phys. Rev. Lett.*, 104:104501, 2010.
33. J. A. Sherratt. An analysis of vegetation stripe formation in semi-arid landscapes. *J. Math. Biol.*, 51:183–197, 2005.
34. M. B. Short and A. L. Bertozzi. Nonlinear patterns in urban crime: Hotspots, bifurcations and suppression. *SIAM J. Appl. Dyn. Sys.*, 9:462–483, 2010.
35. J. V. I. Timonen, M. Latikka, L. Leibler, R. H. A. Ras, and O. Ikkala. Switchable static and dynamic self-assembly of magnetic droplets on superhydrophobic surfaces. *Science*, 341:253–257, 2013.
36. M. Tlidi, R. Lefever, and A. Vladimirov. On vegetation clustering, localized bare soil spots and fairy circles. In *Dissipative Solitons: From Optics to Biology and Medicine*, volume 751 of *Lecture Notes in Physics*, pages 1–22. Springer, Berlin, 2008.
37. P. B. Umbanhowar, F. Melo, and H. L. Swinney. Localized excitations in a vertically vibrated granular layer. *Nature*, 382:793–796, 1995.
38. A. Yochelis, C. Elphick, A. Hagberg, and E. Meron. Frequency locking in extended systems: The impact of a Turing mode. *Europhys. Lett.*, 69:170–176, 2005.
39. Y. R. Zelnik, S. Kinast, H. Yizhak, G. Bel, and E. Meron. Regime shifts in models of dryland vegetation. *Phil. Trans. R. Soc. A*, 371:20120358, 2013.